EXPERIMENTAL AND DEM-BASED ANALYSIS OF LATERAL STRESS AND SOIL PARTICLE DISPLACEMENT UNDER THE ACTION OF A SUBSOILER
/
基于试验和离散元仿真模拟方法对深松铲下土壤侧向应力与侧向位移的研究

Jun GE, Xu ZHU, Chengmao CAO, Liangfei FANG, Yan SUN, Kuan QIN *), Weidong GAO, Junjie LU [1]
School of Engineering, Anhui Agricultural University, Hefei, Anhui/China
Phone: 86-18855102551; E-mail: qinkuan@ahau.edu.cn
Corresponding author: Qin Kuan
DOI: https://doi.org/10.35633/inmateh-76-74

Keywords: *subsoiler, discrete element simulation, soil lateral stress, soil lateral displacement*

ABSTRACT
The lateral stress on the soil in the lateral position during the operation of a subsoiler directly affects the soil displacement and quality of operation. In this study, soil pressure sensors are used to measure the soil lateral stress at the lateral position of the subsoiler in the soil trough, and a discrete element simulation is used to explore the relationship between the change pattern of the soil lateral stress and soil displacement. The test results show that the soil at the lateral position of the subsoiler is subjected to lateral stress, which leads to the generation of lateral displacements. The lateral stress lasts no longer than 3.5 s, the lateral displacement lasts no longer than 3 s, and both exhibit a fluctuating pattern of peaks and troughs over time. The positive peaks are significantly larger than the troughs, indicating that the positive peaks are the main factor generating soil disturbance. The lateral stress and lateral displacement changes are consistent on the timeline, with the lateral displacement moving in the positive (negative) direction when the lateral stress direction is positive (negative). Both values tend to decrease linearly with increasing transmission distance.

摘要
松土机作业过程中土壤侧向应力直接影响土壤位移及作业质量。本研究通过土槽试验，利用土压力传感器测量松土机侧向位置土壤所受侧向应力，并结合离散元仿真探究土壤侧向应力变化规律与土壤位移的关联性。试验结果表明：松土机侧向位置土壤受侧向应力作用产生侧向位移，侧向应力作用时长不超过 3.5 s，侧向位移持续时长不超过 3 s，二者均呈现"波峰-波谷"交替的波动规律，且正向波峰幅值显著高于波谷，表明正向应力峰是引发土壤扰动的主要因素；侧向应力与侧向位移在时序上具有一致性，侧向应力方向为正（负）时，侧向位移沿正（负）方向运动；二者均随传递距离增大呈线性衰减趋势。研究结果为优化松土机结构参数与作业模式提供了理论依据。

INTRODUCTION
Deep-loosening tillage is an effective method for improving soil physical properties and increasing crop yield (*Arvidsson et al., 2010*). The subsoiler disturbs the soil laterally, increasing its ability to hold water and moisture (*Wang et al., 2020*). Lateral disturbances are caused by stresses placed on the soil by the subsoiler when it contacts the soil and are transmitted laterally (*Ibrahmi et al., 2014*). This process is accompanied by soil displacement and deformation, which disrupt the original structure of the soil on both sides of the subsoiler (*Li et al., 2016*).

Scholars around the world have conducted relevant studies (*Li et al., 2023*) to determine how lateral stresses are generated during subsoiler operations and how they affect soil displacement and disturbance (*Ma et al., 2019*). Research has shown that the subsoiler creates lateral stresses on the soil on both sides through shear and compression. *Huang et al. (2016)* further found that the shearing and squeezing of the soil by the subsoiler shovel originated from the shovel tip flanks and that the shearing of the soil by the shovel tip flanks produced soil failure that resulted in soil slippage. Moreover, the stress exerted on the soil increased with proximity to the shovel tip flanks.

[1] *Ge Jun, Lecturer PhD. Eng.; Zhu Xu, M.S. Stud. Eng.; Cao Chengmao, Prof. PhD. Eng.; Fang Liangfei, Lecturer PhD. Eng.; Sun Yan, Assoc. Prof. M.S. Eng.; Qin Kuan*, Assoc. Prof. PhD. Eng.; Gao Weidong, M.S. Stud. Eng.; Lu Junjie, M.S. Stud. Eng.*

Liu et al. (2017) found that lateral stresses caused soil loosening and fragmentation and that soils at different depths were subjected to stresses of different magnitudes. The above findings show that scholars have clearly studied how lateral stresses are generated in the process of deep loosening and that the magnitudes of lateral stresses vary in different locations of the soil. However, it is not clear exactly how lateral stresses change at different soil lateral locations and what the exact magnitudes are. This is important for analyzing how lateral stresses drive the entire lateral soil movement. If the variation rule of the lateral stress at different lateral soil locations can be explored, the lateral soil displacement law can be further analyzed. Scholars have studied soil displacement patterns in deep pine operations. *Ding et al. (2017a)* found that during deep subsoiler operation, the soil above the flanks of the shovel tip was first lifted to the sides along the forward direction of the deep subsoiler after a force was applied. Then, the soil was moved to the sides. The soil below the flanks of the shovel tip was extruded laterally by the subsoiler to form a rectangular groove approximately equal in width to that of the shovel. *Ding et al. (2017b)* and *Hang et al. (2017)* also found that the lateral displacements were significantly greater for shallow soils than for soils in other locations and that deeper soils had the least lateral displacements. *Zhang (2018)* used the discrete element method with a soil trough test to study the effect of a deep subsoiler on soil displacement and found that the disturbance of the soil by the deep subsoiler extends from the tip of the shovel to the surface of the soil on both sides, at which time the soil on both sides forms a soil barrier and moves to both sides under the actions of lateral stresses. However, there is a lack of analysis of the causes of lateral displacement from a force perspective, and it is not clear how lateral stresses specifically affect lateral displacement.

In summary, this study aims to determine both the change rule of the soil lateral stress at the lateral position during the operation of a subsoiler. In this study, using a soil trough and soil pressure sensor in combination with a discrete element simulation test, a fixed-point layered analysis of the lateral position of the soil lateral stress and lateral displacement change rule of the subsoiler is conducted, and the lateral stress change rule of the lateral displacement and perturbation of the impact are analyzed. This provides a theoretical basis for improving the quality of deep pine operations (*Li et al., 2021; Zhang et al., 2021*)

MATERIALS AND METHODS

Test subsoiler

The test subsoiler is a double-wing subsoiler, which consists of two parts: the tip and handle. The tip is the main working part of the subsoiler, the structure and dimensions of which is shown in Fig. 1.

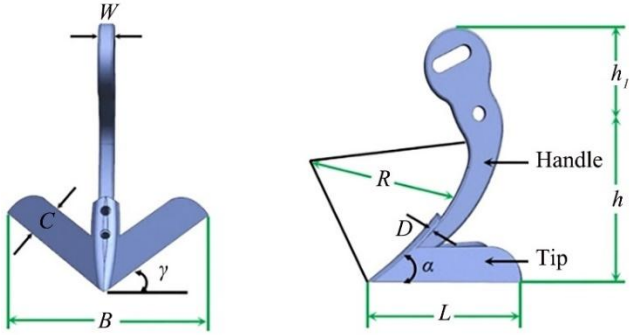

Fig. 1 – Schematic drawing of the subsoiler

In Fig.1, R represents the radius of curvature of the shovel shank in mm. W is the thickness of the shovel shank in mm. $h+h1$ is the height of the tillage tool shank in mm. B is the width of the shovel tip in mm. C is the width of the shovel tip flange in mm. L is the length of the shovel tip flange in mm. D is the thickness of the tillage tool tip in mm. α is the angle of the tangent edge in degrees. γ is the angle of the tillage tool tip flange tension in degrees.

Table 1

Parameters of the subsoiler.

Parameter	*R* (mm)	*W* (mm)	*h* (mm)	h_1 (mm)	*B* (mm)	*C* (mm)	*D* (mm)	*L* (mm)	*α* (°)	*γ* (°)
Value	100	15	160	50	220	30	3	190	30	45

Table 1 shows the tillage tool tip and tillage tool handle structure parameters according to the standard JB/T 9788-1999, “Subsoiler and share shaft”. The subsoiler was made of 65Mn, as specified in GB/T700, and

the blade was quenched to achieve a hardness of 48–56 HRC. The shovel handle was bolted to the shovel tip, and the upper part of the shovel handle contained bolt holes for connecting and fixing it to the test bench.

Soil bin experimental device

Fig. 2 shows the schematic of the test bench and sensor system, which mainly consisted of a soil trough, gear motor, test bogie, bogie guide rail, gears, rack, control cabinet, and subsoiler. The basic parameters of the soil trough were as follows: length = 4,000 mm; width = 1,000 mm; and height = 800 mm. The gear motor provides power for deep-loosening operations. The gear motor was integrated with a 130ST-M15025 servo motor with a power of 3.8 kW and a three-stage gear ratio planetary reducer. The gears were mounted on the output shaft of the reducer for transmission. The gear rack was installed in the side frame of the soil trough, the bogie rail was installed in the side frame on both sides of the trough, the gear motor was fixed to the test bogie, and the test bogie was driven by the gear rack to move in a straight line along the rail.

The bogie moved in the range of 0–1.6 m/s. The subsoiler was fixed to the suspension under the test bogie using bolts and moved forward or backward with the bogie at a uniform speed. No. 8 in Fig. 2 is the self-made sensor-fixing device. The sensor-fixing device has an inverted L-shape structure (300 height × 2 thick, mm). The upper end is bolted to the body frame, and the lower end can fix the sensor. The test sensor adopted was a high-precision cylindrical point-type soil pressure sensor (DMTY model, Nanjing Dan Mor Electronic Technology Co.). This pressure sensor has a diameter of 16 mm, thickness of 4.8 mm, range of 0.05 to 10 MPa, and sensitivity of 2 mV/V. The polished side of the sensor was the stress sensing surface, and the unpolished side was the support surface. The electrical signal collected by the sensor was converted into a pressure value using Equation 1:

$$P_i = K(F_i - F_0) \tag{1}$$

where P_i is the real-time pressure value to which the sensor is subjected (kPa), F_i is the output electrical signal strain value corresponding to P_i in μV, F_0 is the electrical signal strain value output at the sensor's zero point in μV, and K is the sensor calibration factor of 0.152 kPa/μV. The measured pressure values were converted into pressure values using Equation 2:

$$F = P_i \times \pi r^2 \tag{2}$$

where F is the stress collected by the sensor in N and r is the radius of the sensor (8 mm).

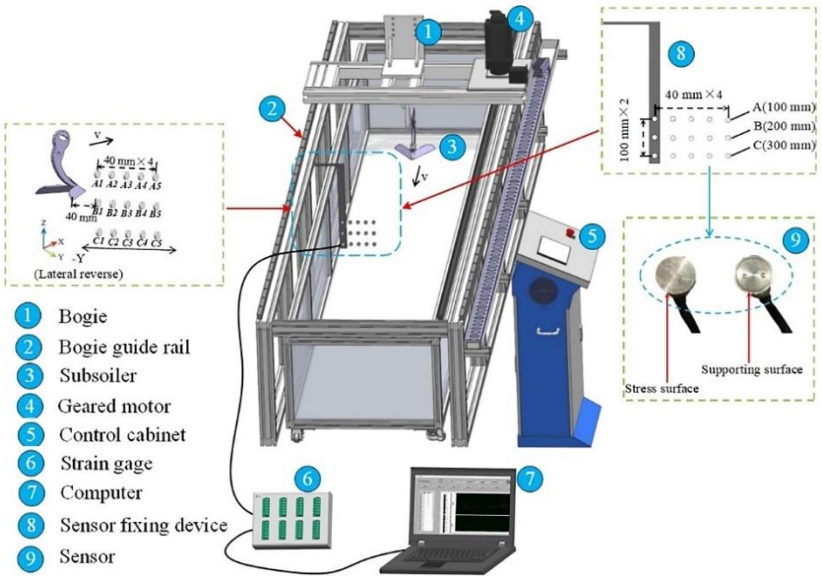

Fig. 2 – Schematic illustration of the soil bin device and sensor system

Soil preparation

The test soil in the soil trough was sandy loam, and the soil physical parameters were determined before the test using a GHHB-009-485-1 soil moisture meter (moisture accuracy ± 0.3% RH), ring knife, and TYD-2 soil firmness meter (accuracy ± 1%) to determine the soil moisture content, bulk weight, and soil firmness in the shallow (soil depth range of 0–150 mm), middle (150–270 mm), and deep (270–320 mm) soil layers, respectively. Table 2 lists the obtained soil water content, bulk weight, soil firmness, and soil physical parameters.

Table 2

Basic physical soil parameters.

Soil depth (mm)	Soil density (kg/m³)	Moisture content (%)	Soil hardness (kg/cm²)
0–150	1310	11.21	14.4
150–270	1420	12.32	16.8
270–320	1610	14.31	20.3

Experimental methods design

The soil at the lateral position of the subsoiler was divided into shallow (0–150 mm), middle (150–270 mm), and deep (270–320 mm) layers. According to its distance from the subsoiler, each layer was further divided into five areas, for a total of 15 areas within the three layers. The test was conducted by burying the sensor in the area above and determining the lateral stress on the soil at the lateral position in a point-by-point manner. The sensor was set up in the soil trough, as shown in Fig. 2, and the sensor was buried at depths in the shallow, middle, and deep layers, corresponding to the depths of layers A, B, and C, respectively. The distances of the sensor from the edge of the wing shovel of the subsoiler used were 40, 80, 120, 160, and 200 mm (in order of 40 mm increases), corresponding to the five lateral positions: 1, 2, 3, 4, and 5. Based on the preliminary pre-test, there is almost no lateral stress response after exceeding a lateral distance of 200 mm. Therefore, the maximum lateral distance determination point was set to 200 mm. The soil pressure sensors were calibrated using a potentiometer-based calibration method prior to testing (*Lamande et al., 2015*). The sensor was buried behind the measurement point and calibrated to zero. As shown in Fig. 3, the operating depth of the subsoiler was 200 mm, and the operating speed was 0.2 m/s during the test. The middle section of the 1,000 mm soil trough was used as the stabilization measurement area. The subsoiler was moved from the beginning of the soil trough to the end of the soil trough for each test stroke. After each test, the subsoiler was reset, the soil in the soil trough was reprepared, and the soil parameters were controlled within 100% ± 5% relative error. Each stroke was repeated five times, and the average value of the test results was taken. The test was completed when all five lateral positions of the soil layers A, B, and C were measured.

The response start time was set to be the point when the first stress change value was captured for each test stroke, and the response cutoff time was when the final stress value stabilized. When all tests were completed, the collected voltage signals were converted to stress values using Equations 1 and 2, and the law of lateral stresses was applied to each lateral position in layers A, B, and C of the soil and obtained as a function of time. During the test, an I-SPEED high-speed camera was used to record the deep pine process and obtain soil disturbance images at specific time points. Fig. 3 shows the high-speed photograph arrangement.

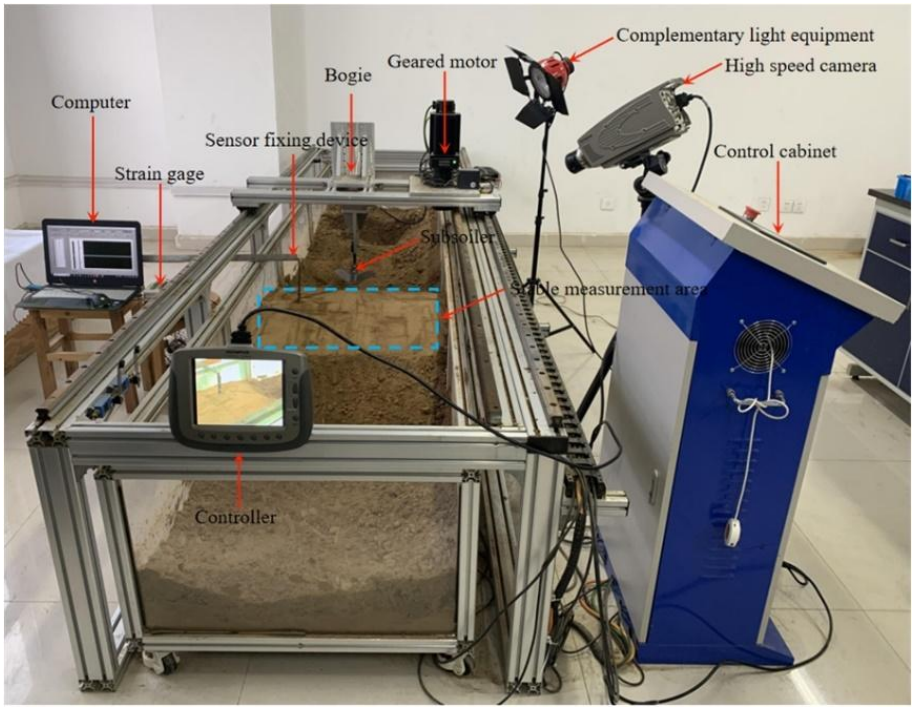

Fig. 3 – Soil trough test procedure

Discrete element simulation

A three-dimensional model of the subsoiler and a soil model identical to the actual soil trough test were created. As shown in Fig. 4, a soil model with a length × width × height of 1,000 mm × 800 mm × 320 mm was created using the EDEM. Shallow soil (0–150 mm) is shown in blue, medium soil (150–270 mm) in green, and deep soil (270–320 mm) in red.

To ensure that the discrete element simulation model was consistent with the actual soil, the Hertz-Mindlin model with the JKR model was selected as the particle contact model. The Hertz-Mindlin (no-slip) contact model between the soil particles and the tip of the subsoiler was selected, and basic spherical soil particles with a radius of 4 mm were chosen for this study.

The established soil model and model parameters were mainly divided into material and contact parameters, which included the density, Poisson's ratio, and shear modulus of the soil and subsoiler (65Mn), which mainly included the friction factor and coefficient of restitution between the materials. The soil density was obtained through actual measurements, and the other parameters were determined from the literature. Table 3 lists the simulation parameters.

Table 3

Basic discrete element model parameters

Parameter	Shallow soil	Middle soil	Deep soil
Soil Poisson's ratio	0.40	0.42	0.43
Soil shear modulus (Pa)	1×10^6	1.4×10^6	1.6×10^6
Soil density (kg/m^3)	1,370	1,492	1,705
Restitution coefficient between soils	0.2	0.2	0.15
Static friction coefficient between soils	0.4	0.4	0.3
Dynamic friction coefficient between soils	0.3	0.3	0.2
Restitution coefficient of soil and 65Mn	0.2	0.2	0.17
Static friction coefficient of soil and 65Mn	0.5	0.5	0.4
Dynamic friction coefficient of soil and 65Mn	0.3	0.2	0.09
Soil surface energy	4.4	5.1	6.2
65Mn Poisson's ratio	0.35		
65Mn shear modulus (Pa)	7.27×10^{10}		
65Mn density (kg/m^3)	7,830		
Total number of soil particles	610,000		
Gravity acceleration (m·s^{-2})	9.81		

The clipping module of the EDEM was utilized to select soil-particle clusters (particle clusters consisting of five soil particles) in the soil model, as shown in Fig. 4, where the soil-particle cluster locations were the same as those of the soil trough test sensor measurement points.

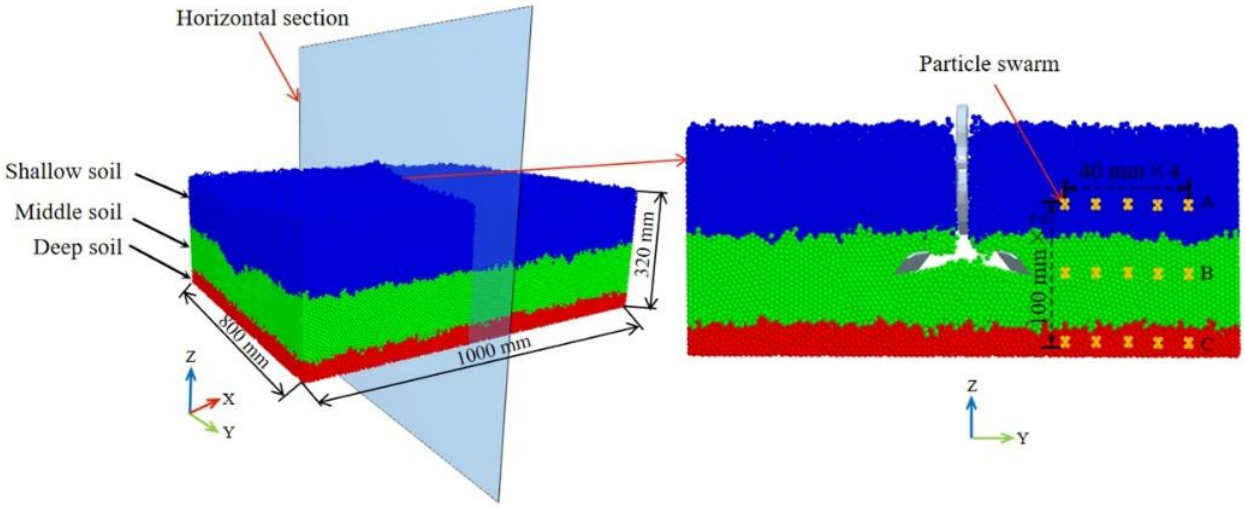

Fig. 4 – Simulation modelling with soil particle swarms

The entire discrete element simulation test procedure was consistent with that of the soil-trough test. After the test, the lateral displacement data of the soil particle population were counted (the data were

averaged) to obtain the change rule of the lateral displacement of the soil at the five lateral positions of the soil in layers A, B, and C. The soil model was also dissected along the lateral direction through the clipping module to observe the disturbance state of the soil at different lateral locations during the deep pine operation.

RESULTS

Basic laws of lateral soil stresses and lateral soil displacements

Fig. 5a shows that lateral stresses are generated during the operation of the subsoiler. The lateral stresses are transmitted to various locations in the lateral soil, and the lateral stresses show a fluctuating pattern with time changes (*Qin et al., 2022*). The entire duration of the fluctuation did not exceed 3.5 s. This result is in agreement with the findings of *El Kahi et al. (2020)* and *Lutz et al. (2017)*, who both found that the lateral stress transfer process in soil can have fluctuating characteristics. Lateral stress fluctuation exists in two cases. The first case is an initial rise and a subsequent fall; that is, the fluctuation only exists at a peak. The second case is an initial rise, a subsequent fall, and a subsequent rise; that is, the curve exists in a peak and a trough. In this case, the value of the wave peak is much larger than that of the trough, which indicates that the wave peak is the main reason for the lateral displacement of the soil affected by the lateral stress.

Fig. 5b shows that the lateral soil displacement caused by the subsoiler exhibited a fluctuating pattern over time and that the entire fluctuation duration did not exceed 3 s. The lateral displacement exhibited the same two fluctuations as those of the lateral stress. This indicates that the two change patterns were consistent in the process of lateral displacement caused by lateral stress.

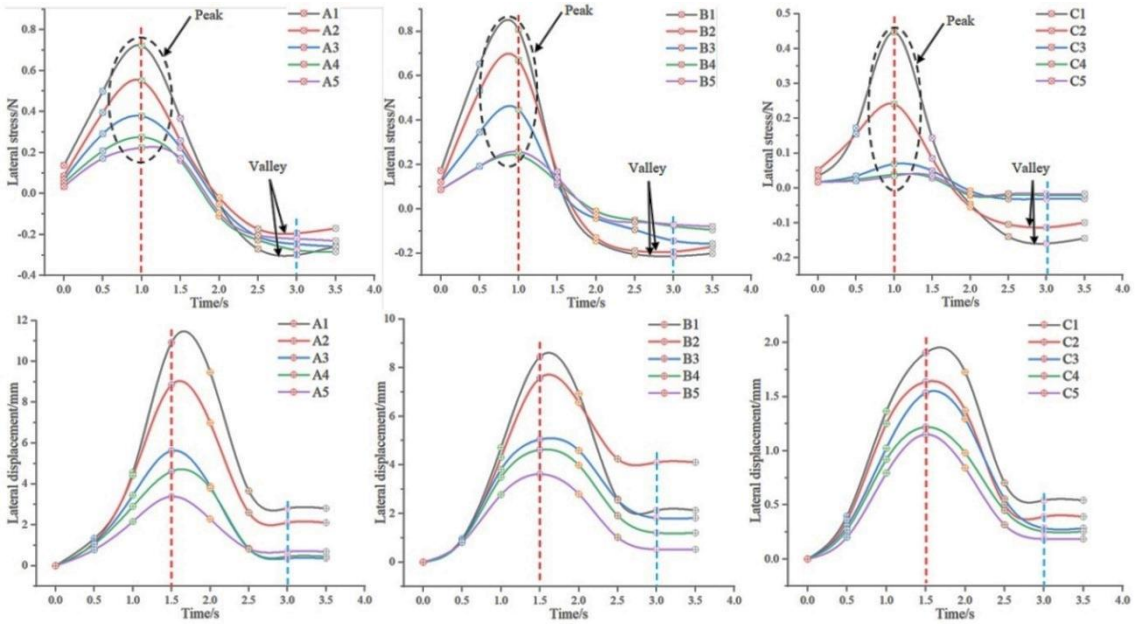

Fig. 5 – Change laws of lateral stress and displacement over time during subsoiler operation

(a) Change law of lateral stress on the soil over time during subsoiler operation

(b) Change law of lateral soil displacement over time during subsoiler operation

Analysis of soil lateral stress and lateral displacement extremes

Fig. 6 illustrates the analysis of the maximum and minimum values of lateral stress and lateral displacement. The maximum values represent the highest points during the variation of lateral stress and displacement and typically occur at the peaks of the waveform. Conversely, the minimum values are the lowest points, occurring at the troughs or endpoints of the waveform. The sign (positive or negative) of each extreme value indicates the direction of the force or displacement, while the magnitude reflects its intensity. As shown in Fig. 6, the maximum (positive) values of lateral stress and displacement are significantly greater in magnitude than the minimum (negative) values. This suggests that positive-direction lateral stress and displacement are dominant over those in the negative direction.

The extreme values of lateral soil stress showed a linear decreasing trend with increasing transmission distance, particularly in soil layers B and C. Similarly, the large (positive) values of lateral soil displacement also decreased linearly with transmission distance, while the small (negative) values of displacement exhibited a linear decrease primarily in the C horizon.

These results indicate that, in the positive direction, both lateral force and displacement effects diminish linearly as the transmission distance increases (*Jude et al., 2012*). However, in the negative direction, no consistent pattern of change was observed.

The maximum and minimum values of lateral force and lateral displacement were analyzed for each layer. In soil layer A, the maximum and minimum values of the lateral force of A1 were the largest, being observed at 0.72 N and -0.30 N, respectively. In layer B, the maximum and minimum values of the lateral force of B1 were the largest, at 0.81 N and -0.21 N, respectively. In layer C, the maximum and minimum values of the lateral force of C1 were the largest, at 0.45 N and -0.16 N, respectively. In layer A, the maximum and minimum values of A1 were 10.93 mm and 2.31 mm, respectively. In layer A, the maximum and minimum values of A1 were 10.93 mm and 2.31 mm, respectively. In soil layer A, A1 had the largest maximum and minimum values of lateral displacement, at 10.93 mm and 2.31 mm, respectively. In soil layer B, B1 had the largest maximum value of lateral displacement and B2 had the largest minimum value, which were 8.44 mm and 3.60 mm, respectively. In soil layer C, C1 had the largest maximum and minimum values of lateral displacement, at 1.91 mm and 0.34 mm, respectively.

From the above results, it can be seen that the maximum extreme value of lateral soil stress occurred in layer B, followed by layer A, and was lowest in layer C. The minimum value of the lateral stress in soil layer A was the highest, followed by those in layers B and C. The maximum extreme values of lateral displacement were observed in layer A, followed by layer B, with the lowest in layer C. In contrast, the highest minimum (negative) values of lateral displacement occurred in layer B, followed by layer A, and were lowest in layer C. Regarding lateral stress, the maximum positive values were recorded in layer B, followed by layer A, and were lowest in layer C. These findings suggest that layer B experienced the highest lateral stress, while layer A exhibited the greatest lateral displacement.

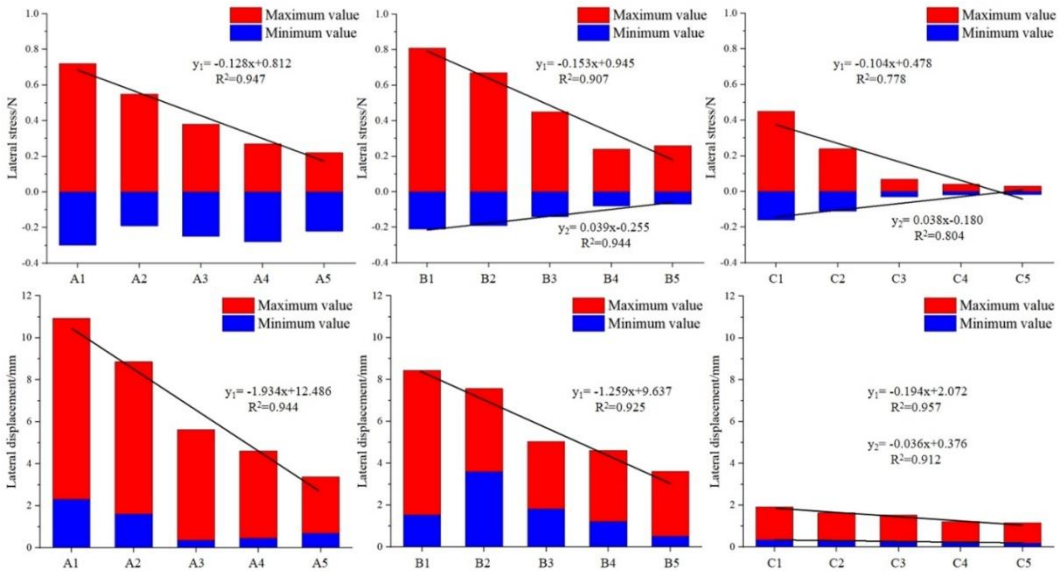

Fig. 6 – Analysis of lateral force and soil displacement extremes

(a) Lateral stress extremes, and (b) Lateral displacement extremes

Timeline correspondence of lateral stresses driving changes in soil lateral displacement

Fig. 7 shows that the lateral stress increases from 0–1 s and decreases from 1.0–1.5 s, and that the direction of the lateral stress is positive from 0–1.5 s. The lateral stress decreases from 0–1.7 s, and the direction of the lateral stress changes from positive to negative. The lateral stress decreases from 1.7–3.0 s, and the direction of lateral stress is negative. The range of 3.0–3.5 s is a special time period in which the phenomenon of lateral stress rebound appeared in the A1, A2, B1, B2, C1, and C2 positions. The direction is still negative, and the lateral stress remains unchanged in the C3, C4, and C5 positions. In the other positions, the lateral stress continues to decrease.

The lateral displacement increased from 0–1.5 s and moved in the positive direction. At approximately 1.7 s, the direction of movement started to change from positive to negative, and from 1.7–3.0 s, the lateral stress started to decrease and move in the negative direction. By 3.0 s, the lateral displacement stopped moving. These results show that lateral displacement and lateral stress remain consistent on the time line.

From 0–1.7 s, the direction of lateral stress is positive, and the lateral displacement moves in the positive direction. From 1.7–3.0 s, the direction of lateral stress is negative, and the lateral displacement moves in the negative direction. The range of 3.0–3.5 s is a special time period in which there is still a change of negative lateral stress at all lateral locations, but the stress is no longer able to push the soil to move laterally.

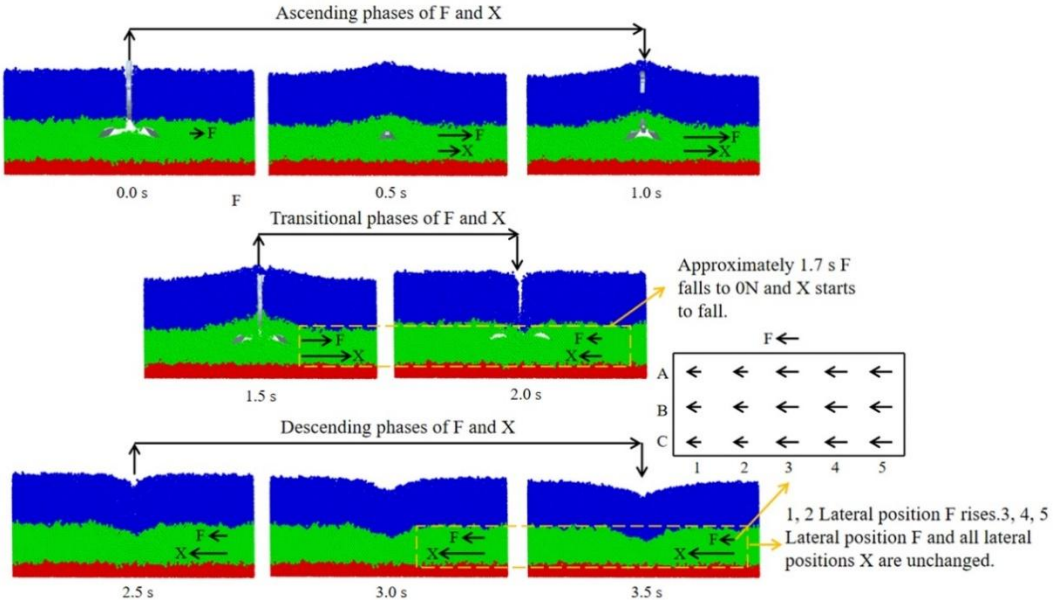

Fig. 7 – Direction of lateral stress and lateral displacement with timeline

Lateral stress and lateral displacement with the time incremental (decremental) change rule of law

Fig. 8a shows that both the increment and decrement of the lateral stress in soil layer B were the largest, and this was followed by those in layers A and C. The maximum increase and decrease in lateral stress in layer B were the largest. The maximum value of the lateral stress increment occurs at position B1 from 0–0.5 s, with a maximum increment of 0.48 N. The minimum value of the decrement occurs at position B1 from 1–1.5 s, with a maximum decrement of 0.66 N. The maximum value of the decrement occurred at position B1 from 1–1.5 s, with a maximum decrement of 0.66 N.

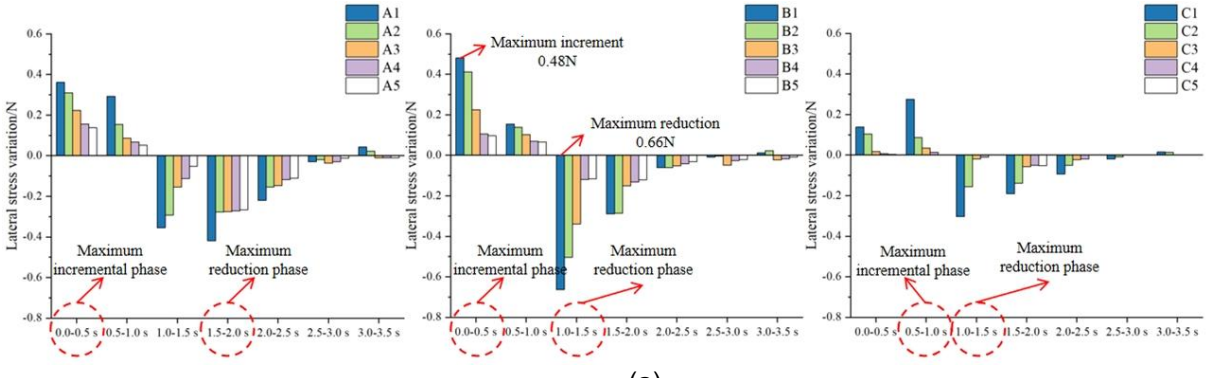

(a)

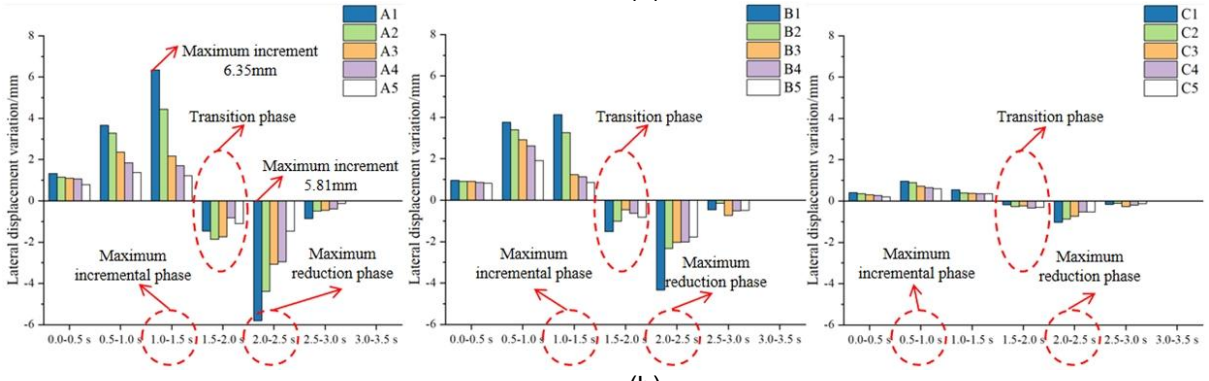

(b)

Fig. 8 – Increase (decrease) in lateral stress and soil displacement at different time intervals

(a) Increase (decrease) in lateral stress at different time intervals

(b) Increase (decrease) in lateral displacement at different time intervals

Both the increment and decrement in the lateral displacement of the soil in layer A were the largest, followed by those in layers B and C. The maximum increment and decrement of the lateral displacement occurred at location A1 from 1.0–1.5 s. The maximum value of the lateral displacement increment occurred at position A1 from 1.0–1.5 s with a maximum increment of 6.35 mm. The minimum value of the decrement occurred at position A1 from 2.0–2.5 s, with a maximum decrement of 5.81 mm.

The above results indicate that the change in the lateral stress on the soil in layer B was the largest; however, this change does not cause the largest change in lateral displacement in layer B, instead causing the largest change in lateral displacement in layer A. In addition, the magnitude of the change in lateral stress does not directly correspond to the magnitude of the change in lateral displacement on the same timeline; e.g., the maximum increment in lateral stress is within the range of 0–0.5 s for layers A and B, but the maximum increment in lateral displacement is caused only in the range of 1.0–1.5 s. The maximum decrements in layers A and B are within the ranges of 1.5–2.0 s and 1–1.5 s, respectively, but the maximum decrement in lateral displacement is caused only within the range of 2.0–2.5 s, which indicates that the change in lateral displacement has a certain hysteresis relative to the lateral stress.

CONCLUSIONS

In this study, the variation patterns of soil lateral stress and displacement at the lateral position of a subsoiler were analyzed using soil trough experiments and discrete element simulations conducted at fixed points.

(1) The peak (positive) values of lateral stress and lateral displacement were significantly higher than their corresponding trough (negative) values. Both positive lateral stress and displacement showed a linear decreasing trend with increasing transmission distance. Among the soil layers, the highest positive lateral stress was observed in the B layer, while the highest positive lateral displacement occurred in the A layer.

(2) The directions of lateral stress and displacement were consistent over time. From 0 to 1.7 s, the lateral stress was positive, and the corresponding displacement occurred in the positive direction. Between 1.7 and 3.0 s, the lateral stress became negative, causing the displacement to shift in the negative direction. From 3.0 to 3.5 s, although the lateral stress remained negative at the lateral position, it was no longer sufficient to induce further lateral soil movement.

(3) The soil in the B layer experienced the greatest change in lateral stress; however, this did not result in the greatest lateral displacement within the same layer. Instead, the A layer exhibited the largest change in lateral displacement. Additionally, the variation in lateral displacement corresponded to the changes in lateral stress, but with a noticeable hysteresis, indicating that the displacement response lagged behind the stress changes.

ACKNOWLEDGEMENT

The authors were supported by Anhui Provincial Natural Science Foundation (2308085ME160).

REFERENCES

[1] Arvidsson, J., Hillerström, O. (2010). Specific draught, soil fragmentation and straw incorporation for different tine and share types. *Soil & Tillage Research,* Vol. 110, pp. 154–160, Sweden.

[2] Ding, Q., Ge, S., Ren, J., Li, Y. He R. (2017a). Characteristics of Subsoiler Traction and Soil Disturbance in Paddy Soil (水稻土深松阻力与土壤扰动效果研究). *Transactions of the Chinese Society for Agricultural Machinery.* Vol. 48, pp 47-56, Nanjing/China.

[3] Ding, Q., Ren, J., BELAL, E., Zhao, J., Ge, S., Li, Y. (2017b). Discrete element analysis of deep loosening process in wet clay rice soils (湿粘水稻土深松过程离散元分析). *Transactions of the Chinese Society of Agricultural Machinery*, Vol. 48, pp. 39-47, Nanjing/China.

[4] El Kahi, E., Deck, O., Khouri, M., Mehdizadeh, R., Rahme, P. (2020). A new simplified meta-model to evaluate the transmission of ground movements to structures integrating the elastoplastic soil behavior – Science Direct. *Structures.* Vol. 23, pp. 324-334, France.

[5] Hang, C., Huang, Y., Zhu, R. (2017). Analysis of the movement behaviour of soil between subsoilers based on the discrete element method. *Journal of Terramechanics,* Vol. 74, pp. 35–43, Yangling/China.

[6] Huang, Y., Hang, C., Yuan, M., Wang, B., Zhu, R. (2016). Discrete Element Simulation and Experiment on Disturbance Behavior of Subsoiling (深松土壤扰动行为的离散元仿真与试验). *Transactions of the Chinese Society for Agricultural Machinery*. Vol. 47, pp. 80-88, Yangling/China.

[7] Ibrahmi, A., Bentaher, H., Maalej, A. (2014). Soil-blade orientation effect on tillage forces determined by 3D finite element models. *Spanish Journal of Agricultural Research*, Vol. 12, pp. 941–951, Tunisia.

[8] Jude, L., Radhey, L. K. (2012). Effect of travel speed and vertical load on the subsoil force and displacement under a smooth steel roller. *Journal of Terramechanics*, Vol. 49, pp. 263–270, USA.

[9] Lamandé, M., Keller, T., Berisso, F., Stettler, M., Schjønning, P. (2015). Accuracy of soil stress measurements as affected by transducer dimensions and shape. *Soil & Tillage Research*, Vol. 145, pp.72–77, Denmark.

[10] Li, B., Chen, Y., Chen, J. (2016). Modeling of soil-claw interaction using the discrete element method (DEM). *Soil and Tillage Research*, Vol. 158, pp. 177–185, Yangling/China.

[11] Li, H., Zhang, Z.G., Xue, J.A., Li, Y.L. (2021). Effect of different tillage practices on soil environment and maize yield and efficiency (不同耕作方式对土壤环境及玉米产量与效益的影响). *Journal of Maize Sciences*. Vol. 28, pp. 70-77, Shanxi/China.

[12] Li, J., Sun, K.P., Zhang, Y.H., Zhang, T.H. (2023). Simulation of Tillage Behavior of Double Winged Subsoiler Based on Discrete Element Method (基于离散元法的双翼深松铲耕作行为的仿真分析). *Journal of Inner Mongolia Agricultural University (Natural Science Edition)*. Vol. 44, pp. 67-75, Yunnan/China.

[13] Liu, X.H., Qiu, L.C. (2017). Finite element simulation analysis of soil cutting by vibratory subsoiler-based on ANSYS/LS-DYNA (振动深松铲土壤切削有限元模拟分析). *Journal of Agricultural Mechanization Research*. 1, pp. 19-24, Shengyang/China.

[14] Lutz, Auersch. (2017). Mitigation of railway induced vibration at the track, in the transmission path through the soil and at the building. *Procedia Engineering*, Vol. 199, pp. 2312–2317, Germany.

[15] Ma, Y., Wang, A., Zhao, J., Hao, J., Li, J., Ma, L., Zhao, W., Wu, Y. (2019). Simulation analysis and experiment of drag reduction effect of convex blade subsoiler based on discrete element method (基于离散元法的凸圆刃式深松铲减阻效果仿真分析与试验). Transactions of the Chinese Society of Agricultural Engineering. Vol. 35, pp. 16-23, Hebei/China.

[16] Qin, K., Zhao, Y., Zhang, Y., Cao, C., Shen, Z. (2022). Lateral stress and its transmission law caused by operation of a double-wing subsoiler in sandy loam soil. *Frontiers in Environmental Science*, Vol.10, No. 986361, Anhui/China.

[17] Wang, Y., Zhang, D., Yang L., & Zhong, X., (2020). Modeling the interaction of soil and a vibrating subsoiler using the discrete element method. *Computers and Electronics in Agriculture,* Vol. 174, No. 105518, Nanjing/ China

[18] Zhang, S.L. (2018). Simulations and experiments of soil disturbance as affected by the dislocation arrangement of subsoilers (深松铲错位布置对土壤扰动影响的仿真与试验研究). *North West Agriculture and Forestry University,* Dissertation, Yangling/China.

[19] Zhang, Z., Gan, S., Zuo, G., Tong, J. (2021). Bionic Design and Performance Experiment of Sandfish Head Inspired Subsoiler Tine (以砂鱼蜥头部为原型的仿生深松铲尖设计与离散元仿真). *Transactions of the Chinese Society of Agricultural Machinery*. Vol. 52, pp. 33-42, Yunnan/China.